# Chapter 5
# Topologically Non-trivial Magnetic Skyrmions in Confined Geometries


**Haifeng Du and Mingliang Tian**

**Abstract** Magnetic skyrmion is a small magnetic whirl that possesses non-trivial topology and behaves like a particle. The specially twisted spin arrangement within skyrmion gives rise to topological stability and low critical current to drive its motion, both of them benefit the potential technological application in memory devices. In this chapter, we briefly introduce the notation of topology of magnetic skyrmions and recent progress ranging from the hard disk storage in conventional magnetic memory device to racetrack memory by using magnetic skyrmions. The related magnetic phases in skyrmion materials based on the Dzyaloshinskii-Moriya (DM) interactions are discussed in detail. Furthermore, experimental achievements for the formation and stability of highly geometry-confined skyrmions are outlined, where the topological effects are fully embodied.

## 5.1 Introduction

Magnetic memory devices mainly magnetic hard disk drives (HDD) have been the primary repository of digital data for more than half a century. Data is recorded in a thin ferromagnetic film with the binary data bits 0 and 1 represented by the direction of magnetization of a small domain (Fig. 5.1). Data read from the disk is accomplished by transferring the magnetization of the small magnetic domain into electric signals via the giant magnetoresistance (GMR) effect, while writing data is accomplished by using the magnetic field to control the direction of the small magnetic domain. In spite of its extreme success in memory device, the decreased size of the magnetic domains in HDD may lead to the loss of their magnetic state due to the thermally

H. Du · M. Tian (✉)
The Anhui Province Key Laboratory of Condensed Matter Physics at Extreme Conditions, and High Magnetic Field Laboratory, Chinese Academy of Science (CAS), Hefei 230031, Anhui, China
e-mail: tianml@hmfl.ac.cn

H. Du · M. Tian
School of Physics and Materials Science, Anhui University, Hefei 230601, Anhui, China



S. Gupta and A. Saxena (eds.), *The Role of Topology in Materials*,
Springer Series in Solid-State Sciences 189,
https://doi.org/10.1007/978-3-319-76596-9_5

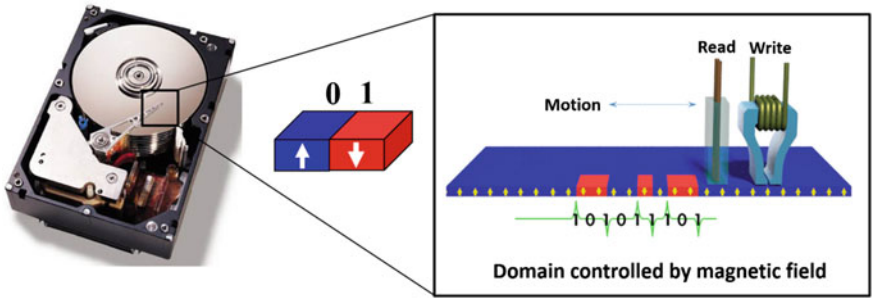


**Fig. 5.1** Hard disk drive and an overview of how it works

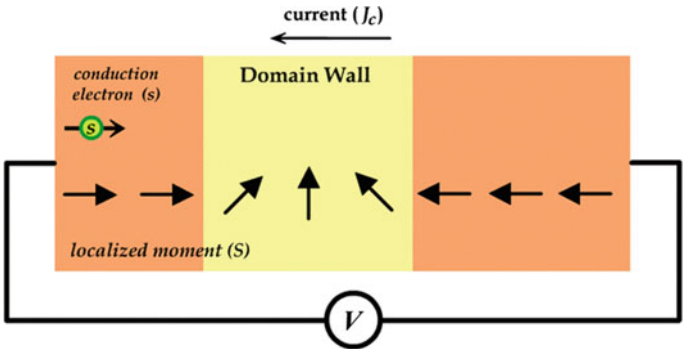


**Fig. 5.2** Spin transfer torque effect in which the orientation of localized magnetic moments can be controlled by using a spin-polarized current

induced magnetic instability, commonly known as the superparamagnetic limit [1]. Meanwhile, the movable mechanical engines consume large energy and thus set a limitation on their writing/reading speed.

Therefore, a number of alternative magnetic memory architectures towards achieving high reliability, performance and capacity data storage have been proposed. A typical one is based on controllable manipulation of magnetic domain walls (DW) by using electrical current [2]. It is well known that electrons carry not only charges but also spins. In a non-ferromagnetic material, the spins of electrons are generally randomly oriented and do not show spin polarization. However, when a ferromagnetic (FM) component is incorporated into a device, a spin-polarized current is produced when a current passes through the FM component with fixed magnetization direction, i.e. fixed layer. If this spin-polarized current is further passed into a second thinner magnetic layer (the "free layer"), its orientation of the magnetization can be changed due to the transformation of angular momentum of electrons to this FM layer. This effect is the so-called spin transfer torque (STT) (Fig. 5.2a), and can be used to flip the orientation of the magnetic domains. This means that domain walls can be moved by spin polarized current.

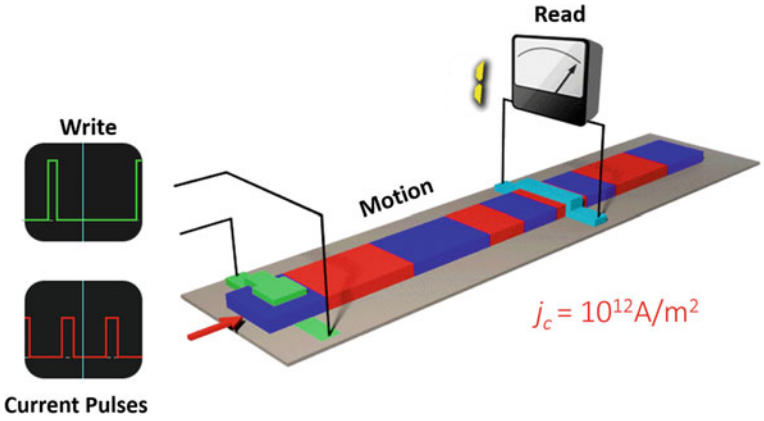


**Fig. 5.3** Racetrack memory and an overview of how it works

Based on this effect, a memory device was then proposed by IBM and called racetrack memory (RM) that actually inherited the bubble memory concept [3]. In the RM (Fig. 5.3), the information bit (0 or 1) is encoded in magnetic domains separated by domain walls (DWs) that can move by means of a spin polarized current. A read/write device is fixed somewhere to polarize or measure the magnetization in a given domain. By controlling current pulses in the device, the domain walls can be moved at speeds of hundreds of miles per hour and then can be stopped precisely at the position needed, allowing massive amounts of stored information to be accessed in less than a billionth of a second. The advantage of data access speed makes the racetrack memory so intriguing. Projections are that the racetrack memory can read or write a bit of information in less than 1–10 ns, depending on the length of the racetrack, while a hard drive performs the same operation in 3,000,000 ns. However, because the RM based on STT effect requires very high current density ($j_c \sim 10^{12} A/m^2$) to move the domain walls, together with many other physical and material problems such as the pinning effects, the Walker limit, the conventional DW-based RM turned out too complicated to be competitive compared to HDDs. Increasing efforts and resources dedicated to the development of the racetrack memory are then highly required.

In magnets without inversion symmetry, so called chiral magnets, relatively weak spin-orbit coupling leads to the formation of smooth twisted magnetic structure with a long period. Recently, a new local magnetic state, named magnetic skyrmion was discovered in chiral magnets. It has a series of advantages that might allow the device to be more robust and more efficiently manipulated with currents. Here, we will give a brief introduction to the magnetic skyrmions. In Sect. 5.2, we review the topological effect related to magnetic skyrmions. In Sect. 5.3, we concentrate on the formation mechanism of magnetic skyrmions. In the last section, we turn to some special properties of geometrically-confined skyrmions.

## 5.2 Topological Effect in Magnetic Skyrmions

### *5.2.1 Topology in Magnetic Materials*

Traditionally, study on magnetism has mainly followed the route by exploring its microscopic magnetic structure, corresponding properties, and then to realize certain functionality. However, there is now increasing interest to design, predict and fabricate novel materials with particular property and functionality by delineating the active role of topology and geometry. The topology class is mathematically characterized by the homotopy theory [4]. The emergent state possesses a property that is protected in a symmetry sense, and then can be rigorously defined by its corresponding mathematical topological characteristics. One of the important notions in the homotopy theory is the topological defect, which is a stable configuration of matter formed in the very early universe and characterized by a homotopy class. Such configurations are in the original, symmetric or old phase, but they persist after a phase transition to the asymmetric or new phase is completed. There are a number of possible types of defects in a magnetic system. To distinguish these topological defects belonging to one and the same homotopy class, it is convenient to define a global parameter, named as winding (also skyrmion) number, $Q$. Such a parameter is provided by the degree of a mapping $f$: $M \rightarrow N$, where $M$ and $N$ are orientable and compact manifolds, respectively. In the case of both manifolds belonging to n-spheres, the winding number of the mapping, deg $f$, counts how many times $M$ is wrapped around $N$ under the map $f$. In two dimensional case, the easy-plane spin varies as $\boldsymbol{m}(\tau) = (\cos \Phi(\tau), \sin \Phi(\tau))$, where $0 \leq \tau \leq 2\pi$ parameterizes the loop and continuity requires $\boldsymbol{m}(0) = \boldsymbol{m}(2\pi)$, the winding number can be expressed as

$$Q = 1/2\pi \int_0^{2\pi} \partial_\tau \Phi d\tau \tag{5.1}$$

In fact, before the discovery of magnetic skyrmions, this topology method has been used to analyze the complex switching processes observed in ferromagnetic nanoparticles [5]. The switching process involving the creation, propagation, and annihilation of domain walls with complex internal structure. But, from the topological viewpoint, these complex domain walls are composite objects made of only two or more elementary defects: vortices with integer winding numbers ($Q = \pm 1$) and edge defects with fractional winding numbers ($Q = \pm 1/2$). The simplest domain walls are composed of two edge defects with opposite winding numbers. Creation and annihilation of the defects are constrained by conservation of a topological charge. The elementary topological bulk and edge defects will significantly affect the interaction and domain trajectory in the nanowires. For example, head-to-head and tail-to-tail magnetic domain walls in the nanowire are two fundamental domains that behave as free magnetic monopoles carrying a single magnetic charge. They

attract one another since adjacent walls always carry opposite charges, leading to annihilation of the two domain walls. However, the topological edge defects that have the same winding number suppress annihilation of the walls because of a short-range repulsive interaction [6].

In three-dimensional case, $Q$ is the number of spins winding around the unit ring after going through the magnetic ring. It can be done by wrapping the spin vector, $\boldsymbol{m}$ around a unit sphere, where the $Q$ is defined as follows:

$$Q = 1/4\pi \int \boldsymbol{m} \cdot \left(\partial_x \boldsymbol{m} \times \partial_y \boldsymbol{m}\right) dxdy \tag{5.2}$$

According to these definitions, the winding number $Q$ of each configuration also characterizes the number of magnetic monopoles therein.

### 5.2.2 *Topological Stability of Magnetic Skyrmions and Emergent Magnetic Monopoles*

In magnetic materials, a notable example of a topologically stable object is the skyrmion [7–10]. It is a swirl-like spin texture, in which the magnetic moments point in all directions wrapping a unit sphere (Fig. 5.4a). It is then easy to obtain a unit topological charge (Fig. 5.4c) according to (5.3), while it is zero for conventional spin textures like the ferromagnetic state. It explained the topological stability of magnetic skyrmions. Two objects or configurations are topologically different if they belong to a different homotopy group if there exists no continuous transformation of one configuration into the other without cutting or gluing. The same applies to skyrmions: skyrmion lattices in chiral magnets can be regarded as macroscopic lattices formed by topological entities with particle-like properties where the particle-like character of the skyrmions is reflected in the integer winding number of their magnetization.

It must be noted that a non-trivial topology does not imply in itself energetic stability. There is in fact unnecessary relation between topology and energetic stability. Topological stability referred to a system going from one topological state to another is always accompanied by a discontinuity in the continuous field and is only a mathematical concept. For instance, a torus going into a sphere, a rupture must be created on some part of the torus's surface. In this case, the torus would be mathematically described as topologically stable. By contrast, energy stability is always connected to real physical systems and is described by the free energy, which is required to create the rupture and is always finite. That is to say, the mathematical concept of topology is only used to describe a physical system. The attributes of the system including the energy stability depend on the system's physical parameters. To build an efficient link between topological and energy stability, a non-zero phenomenological field rigidity, which is used to account for the finite energy needed to rupture the field's topology, should be introduced. By calculating a breakdown energy-density of the field, a topology-related energy barrier is introduced. For the magnetic skyrmions,

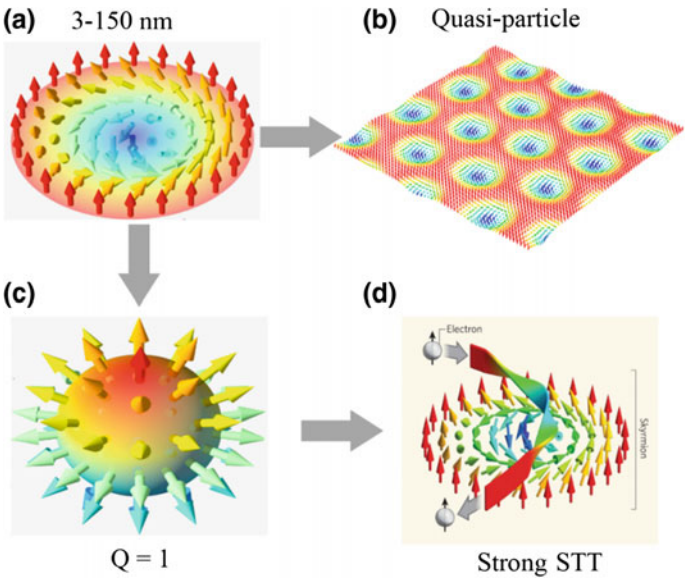


**Fig. 5.4** Magnetic skyrmion and its properties. **a** The spin configuration of single skyrmion. **b** skyrmion lattice. **c** Unit topological charge of skyrmion due to the nontrivial spin arrangement. **d** Strong spin transfer torque effect (STT)

such a topological barrier is extracted by evaluating the energy routine during the transition of the skyrmion number or topological charge in the dynamical process of a skyrmion creation or annihilation. In fact, the barrier height linked to the topological charge has been theoretically calculated [11].

Leaving the energy stability out of consideration, transition between different topological classes can lead to some exotic topological state. For the topology-protected magnetic skyrmions, they cannot be destroyed or created by smooth deformation of other trivial spin textures such as the ferromagnetic state, helical or conical phase. Then what will be happen when the topological winding in a skyrmion can be destroyed. By using a magnetic force microscope (MFM) to map out the distribution and shape of the skyrmions on the surface of the bulk chiral magnets $Fe_{0.5}Co_{0.5}Si$ [12], the field evolution of magnetic states in the sample surface is revealed. The skyrmions disappeared as the magnetic field was reduced to zero and were seen to decay by coalescing with their neighbors to form lines on the surface. At zero magnetic field, the lines created a tiger-stripe pattern. But, there is no individual skyrmion within the bulk of the sample. Computer simulations well reproduced the experimental observation that a similar coalescence occurs beneath the surface. It is then well established that the formation and destruction of magnetic skyrmions is driven by the creation and motion of singular defects. The singular points can be identified with emergent monopoles.

### 5.2.3 Topological and Skyrmion Hall Effect

As a result of their unique spin topology, magnetic skyrmions provide a platform to study many intriguing real-space topological transport phenomena. A well-known example is the Hall effect, which may show a peculiar behavior arising from non-trivial spin arrangements. The ordinary Hall effect of a conductor in a perpendicular magnetic field originates from the Lorentz force acting on the charge carriers. It is usually measured as a voltage transverse to the current. In ferromagnetic conductors, an additional anomalous Hall effect (AHE)—for which the theories usually assume a collinear spin structure—arises from magnetization and spin–orbit interaction and is present even in zero magnetic field. However, in a non-coplanar spin configuration the spin chirality of three magnetic moments spanning a triangle can induce a finite Berry phase and an associated fictitious magnetic field. This field generates an AHE even without the spin–orbit interaction, the so-called topological Hall effect (THE) [13, 14]. Thus, the Berry phase reflects the chirality and winding number of the knots. The topological Hall effect arises besides the normal Hall effect. The topological Hall resistivity is proportional to the density of emerging magnetic field, which is the average density of magnetic field that is associated with the flux quanta $\Phi_0$ contained in the skyrmion of diameter $R$. The strength of emergent magnetic field can be as large as $\langle \boldsymbol{b}_z \rangle \approx 100$ T given a skyrmion of 10 nm in diameter, which thus provides a unique platform to study the high magnetic field response of electrons. Meanwhile, based on the well-known Faraday's law, the motion of a magnetic skyrmion thus produces a time-dependent electric field $\langle \boldsymbol{E}_t \rangle$ that leads to the emergent electromagnetic induction. These effects have been observed in bulk chiral magnets including MnSi, GeMn [15].

Another interesting phenomenon is the skyrmion Hall effect [16, 17]. Because magnetic skyrmion behaves like a particle with a unit topological charge $Q = \pm 1$. Similar to the transverse deflection of charged particles as a result of Lorentz force, the motion of magnetic skyrmion exhibits a well-defined transverse component as a result of topological Magnus force. The skyrmion hall effect is directly related to the device applications. Since skyrmions can be shifted by electrical currents and feel a repulsive force from the edges of the magnetic track as well as from single defects in the wire, they can move relatively undisturbed through the track. This is a highly desired property for racetrack devices, which are supposed to consist of static read- and write-heads, while the magnetic bits are shifted in the track. However, another important aspect of skyrmion dynamics originates from skyrmion Hall effect is that the skyrmions do not only move parallel to the applied current, but also perpendicular to it. This leads to an angle between the skyrmion direction of motion and the current flow called the skyrmion Hall angle. As a result, the skyrmions should move under this constant angle until they start getting repelled by the edge of the material and then keep a constant distance to it. Recent investigation has proved that the billion-fold reproducible displacement of skyrmions is indeed possible and can be achieved with high velocities. Furthermore, it turned out that the skyrmion Hall angle depends on the velocity of the skyrmions, which means that the components of the motion

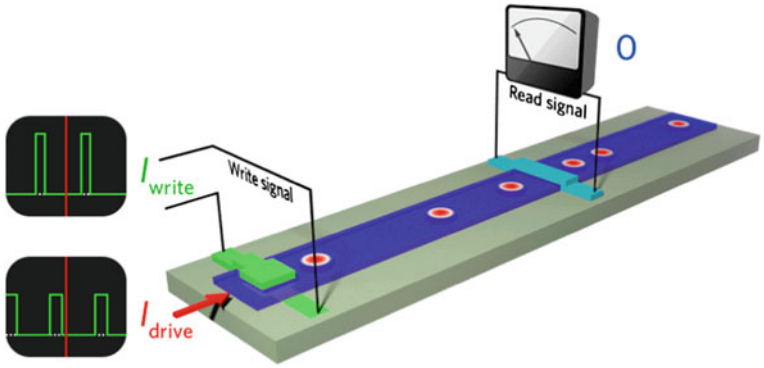


**Fig. 5.5** Skyrmion-based Racetrack memory

parallel or perpendicular to the current flow do not scale equally with the velocity of the skyrmions. This is not predicted in the conventional theoretical description of skyrmions. Part of the solution of this unexpected behavior could be the deformation of the skyrmion spin structure, calling for more theoretical effort to fully understand the properties of skyrmion in confined geometries.

### *5.2.4 Skyrmion-Based Racetrack Memory (RM)*

The peculiar twists of the magnetization within the skyrmion give rise to a nontrivial topology so that the spin current is able to efficiently couple with skyrmion. This process further links to the topological Hall effect and efficient spin-transfer torque effect. As a consequence, the critical current density to drive skyrmions is 4 or 5 orders of magnitude lower than that needed to move the conventional ferromagnetic domain walls. Moreover, the single skyrmion possesses much smaller size than a conventional domain. The typical value of the size is on the order of 3–150 nm depending on the intrinsic parameters of skyrmion materials. These properties including small size, high stability and mobility all benefit to build future skyrmion-based RM [18]. Recent investigations have demonstrated the current-induced creation and motion as well as electric detecting of individual skyrmions in confined geometries even at room temperature [19]. These advances raise great expectations for realizing skyrmion-based RM (Fig. 5.5).

## 5.3 Origin of Magnetic Skyrmion

### *5.3.1 Magnetic Phase Diagram in Chiral Magnets*

Within the framework of micromagnetism that is the continuum theory of magnetic moments, the magnetic microstructure is determined by the couplings among local magnetic moments. Among them, the common one is the exchange interaction. It is a purely quantum phenomenon, which has no analogy in the classical world. The magnetic moments and spontaneous magnetization are realized by the exchange interaction between electrons. In a simple two-electron picture, exchange gives rise to ferromagnetic or antiferromagnetic coupling depending on the sign of exchange constant $J$. In the discrete model, the most general expression for two sites exchange energy between neighboring magnetic moments $\mathbf{S}_i$ and $\mathbf{S}_j$ is:

$$E_e = -J\mathbf{S}_i \cdot \mathbf{S}_j \tag{5.3}$$

Although the exchange interaction keeps spins aligned, it does not align them in a particular direction. This is accomplished by the magnetic anisotropy. Without magnetic anisotropy, the spins in a magnet randomly change direction in response to thermal fluctuations and the magnet is superparamagnetic. There are several kinds of magnetic anisotropy, the most common of which is magnetocrystalline anisotropy. This is a dependence of the energy on the direction of magnetization relative to the crystallographic lattice. Another common source of anisotropy can be induced by internal strains or interface. Single-domain magnets also can have a shape anisotropy due to the magnetostatic effects of the sample shape. This also belongs to stray field energy, which is connected with the magnetic field generated by the magnetic body itself. It arises because each magnetic moment in a ferromagnetic sample represents a magnetic dipole and therefore contributes to the total magnetic field inside the sample.

A magnetic moment will try to reduce its energy by aligning itself parallel to an external magnetic field. The energy that describes the interaction of a magnetic moment with an applied field $\mathbf{B}$ is called Zeeman energy:

$$E_h = -\mathbf{S}_i \cdot \mathbf{B} \tag{5.4}$$

Zeeman energy as well as anisotropies are local energy terms because their energy contributions are determined only by the local values of magnetization vector.

The magnetic structures are determined by the competition among different energies. These naturally lead to non-collinear spin textures such as magnetic domain walls, magnetic vortices and magnetic bubbles. Unlike the controllable manipulation of magnetic domains using magnetic field in the HDD, these non-collinear spin textures may provide new opportunities for the spintronic devices because spins of conduction electrons can efficiently couple with the localized spin textures via a spin angular momentum transfer, the so-called spin transfer torque (STT) mechanism.

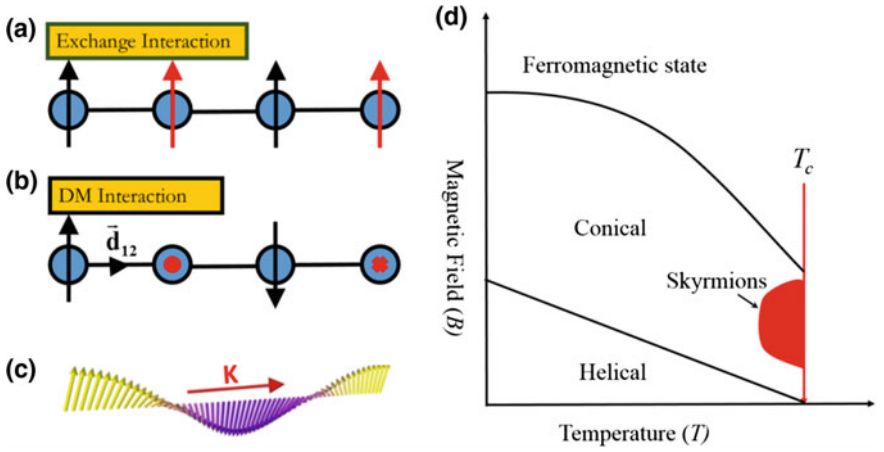


**Fig. 5.6** Magnetic phases in B20 chiral magnets. The competition between ferromagnetic exchange in (**a**) and non-collinear DM interactions in (**b**) leads to a helical ground state in (**c**), which unpins under the application of a high magnetic field to form the conical phase with its wave vector along the direction of magnetic field, and then condenses into a skyrmion crystal with a hexagonal arrangement if temperature is close to the Curie temperature $T_c$. Images are taken from [24]

The formation and stabilization of magnetic skyrmions often require some non-collinear magnetic interactions. A typical one is the Dzyaloshinskii-Moriya (DM) interaction [20]. In addition to this coupling, it has also been addressed that magnetic dipolar interaction, frustrated exchange interaction [21], and four-spin exchange interaction [22] are all able to create skyrmions. Among them, the DM-induced skyrmions have evident advantages including small and tunable size [23], and extra stability even in highly confined geometries [24]. Due to the importance of DM couplings, it is valuable to introduce its origin before entering the non-collinear magnetic structures in chiral magnets. DM interactions come from the symmetry-breaking in the crystal lattice or interface and surface. It is written as [25]:

$$E_D = \mathbf{D}_{ij} \cdot \left(\mathbf{S}_i \times \mathbf{S}_j\right) \tag{5.5}$$

Vectors $\mathbf{D}_{ij}$ are the nearest neighbor DM coupling constants and originate from the symmetry-breaking in the crystal lattice. It is obvious that spins tend to be perpendicular to each other under the DM interaction according to (5.5) (Fig. 5.6b). Competition between ferromagnetic and DM interaction leads to a helical ground state (Fig. 5.6c). Since DM interaction is coupled to the lattice, it is chiral. The corresponding magnetic materials are also called chiral magnets. Including the above-mentioned Heisenberg exchange and Zeeman energies, the total energy of a B20 helimagnet with the magnetization $\mathbf{S}$ in the continuum limit can be written as

$$E = J\,(\nabla \mathbf{S})^2 + D\mathbf{S} \cdot (\nabla \times \mathbf{S}) - \mathbf{B} \cdot \mathbf{S} \tag{5.6}$$

The emergent magnetic structures in helical magnets can be well explained within the above-mentioned physical model concerning the DM, ferromagnetic exchange, and external magnetic interaction. The spin helix is created by the completion between DM and ferromagnetic exchange interactions. The wave-vector **k** is fixed depending on the high symmetry crystal axis (Fig. 5.6a–c). Under the action of a magnetic field **B**, a conical phase with **k** ∥ **B** is energetically favorable when the magnetic field is of moderate strength and the temperature *(T)* is lower than the Curie temperature $T_c$. A higher field will further transfer the conical phase into a ferromagnetic state. Because the rotation sense of both helical and conical states orients along only one direction, they are called single-twist magnetic structure. By contrast, magnetic skyrmion is a vortex-like magnetic structure with the magnetization within the skymion rotating in two directions. Skyrmion thus belongs to double-twist modulated magnetic configuration. In bulk materials, the formation of the skyrmion state is commonly explained by the thermal fluctuation effect, where skyrmions occupy only a small temperature-magnetic field *(T-B)* region in the magnetic phase diagram. The magnetic phase diagram in Fig. 5.6d represents a common behavior in B20 helical magnets.

On the contrary, highly stable magnetic skyrmions can be realized by the reduced dimensionality of helical magnets. It has been confirmed experimentally that thin plates of B20 magnets with its thickness around the featured skyrmion size can hold a skyrmion in significantly extended *T-B* phase region even to the zero temperature [26]. The extended skyrmion state in low dimensional B20 magnets has been explained by several different mechanisms. The spatial confinement effects is the first one [27]. Numerical calculation showed that a type of 3D skyrmion, instead of conventional 2D case, appears if the thickness of the film is below a threshold. A 3D skyrmion is characterized by a superposition of double-twist rotation of magnetic skyrmions in the perpendicular plane and conical modulations along the skyrmion axis. The 3D skyrmion is proposed to be energetically favorable and then thermodynamically stable in a broad *T-B* range. The high stability of magnetic skyrmions in 2D materials such as mechanically thinned flakes and quasi-2D MnSi nanostripes can be well explained by this mechanism [28]. Beyond 3D-modulated configuration, highly stable skyrmions can also exist in magnetic materials with the uniaxial magnetic anisotropy [29]. In this case, if the external magnetic field is applied along the direction of easy axis of the system, the energy of conical phase would be significantly increased under a combined action of magnetic field and uniaxial anisotropy. Skyrmion state is thus energetically favorable in large regions of *T-B* space. But, it should be noticed that the skyrmion size and crystal lattice constant are also depend on the strength of uniaxial anisotropy. However, there is no clear experimental evidence to identify this mechanism. For a thin film with uniaxial anisotropy, if the external magnetic field is applied in the film plane, extended elliptic skyrmion gratings are proposed to be energetically favorable if the hard axis of the system is perpendicular to the film plane. In the highly confined helical magnets, the experimental observations, as discussed below, cannot be explained by independently using the three mechanisms.

### 5.3.2 Mechanism of DM Interaction

Magnetic skyrmions were first discovered in metallic alloy MnSi by neutron scattering [8], and later confirmed in semiconductor $Fe_{0.5}Co_{0.5}Si$ by Lorentz Transmission Electron Microscopy (TEM) [9]. Both materials belong to the same lattice class of B20, a non-centrosymmetric binary structure, in the Strukturbericht Symbol. Subsequent investigation proved that the emergence of skyrmion is a common feature in other B20 magnets such as FeGe and $Cu_2OSeO_3$ [28, 31]. The continuing discovery of more skyrmion materials is unambiguously an important and urgent task for the development of skyrmion science. To guide the search for more skyrmion materials, it is instructive to classify all possible materials with DM interaction by symmetry. The pioneering phenomenological theory was introduced by Bogdanov et al. [32], where the technique of symmetric tensor is employed [33, 34] and the classification of point groups hosting skyrmions is achieved [35].

In detail, the Fourier component of the Heisenberg exchange is given by $E_{Hei}(\mathbf{k}) = J\mathbf{k}^2 |\mathbf{S}_\mathbf{k}|^2$, where $\mathbf{S}_\mathbf{k}$ is the Fourier component of the spin $\mathbf{S}_\mathbf{k} = \frac{1}{V}\int d\mathbf{r}\mathbf{S}(\mathbf{r}) \exp(i\mathbf{k}\cdot\mathbf{r})$. Under rotations, $\mathbf{S}$ transforms in the same way as $\mathbf{k}$. As a result, $E_{\mathrm{Hei}}(\mathbf{k})$ is rotationally invariant. Furthermore, the inversion and mirror symmetries are also respected. Therefore this is a generic quadratic term for all ferromagnets. On the other hand, the DM interaction provides a linear term in momentum; $E_{\mathrm{DM}}(\mathbf{k}) = iD\mathbf{S}_\mathbf{k} \cdot (\mathbf{k} \times \mathbf{S}_{-\mathbf{k}})$. Although the rotational symmetry is still preserved, the inversion symmetry is apparently broken, which is the well-known origin of the DM interactions. However a long overlooked fact is the broken mirror symmetry in this DM interaction. This comes from the fact that $\mathbf{S}_\mathbf{k} \cdot (\mathbf{k} \times \mathbf{S}_{-\mathbf{k}})$ is a pseudoscalar. Under any improper rotation such as mirror reflection in the lattice, this term flips sign, and should be ruled out in the energy. This term is a unique feature of lattices, such as T23 group, with only pure rotations. Now a question arises whether this form is the only allowed term linear in $\mathbf{k}$ for any other material.

To answer this question, we can rewrite any k-linear term as a tensor product

$$E_{\mathrm{DM}}(\mathbf{k}) = id_{ijm}k^i S^j_{-\mathbf{k}} S^m_\mathbf{k}, \tag{5.7}$$

where $d_{ijm}$ is a third order tensor that can be constructed from symmetry analysis. Any symmetry operation $R$ can be represented as a $3 \times 3$ matrix in natural basis (x, y, z). Under such operation, vector $\mathbf{k}$ transforms as $k_i \to k_j R_{ji}$, while the pseudovectors $\mathbf{S}_{\pm\mathbf{k}}$ transform as $S_i \to |R| S_j R_{ji}$, where $|R|$ is the determinant of R matrix. If $R$ is an improper rotation, $|R| = -1$. Once $R$ is a symmetry operation, energy should be invariant under such rotation, therefore the tensor $\mathrm{d_{ijm}}$ must satisfy the Neumann's principle:

$$d_{ijm} = R_{ip}R_{jq}R_{mr}d_{pqr} \tag{5.8}$$

In practice, one does not need to go through all symmetry operations in order to determine the $d$ tensor. Most operations can be written as products of some

independent matrices, called generating matrices [36], within the same point group. For T23 point group, the generating matrices are $C_2$and $C_3$ rotations. The Neumann's principle thus leads to the constraint that $d_{xyz} = d_{yzx} = d_{zxy}$, and $d_{xzy} = d_{yxz} = d_{zyx}$. One can symmetrize these parameters by $d_{xyz} = S + D$ and $d_{xzy} = S - D$. However because the whole Hamiltonian can be reorganized as $\sum_{\mathbf{k}} H_{DM}(\mathbf{k}) = \sum_{\mathbf{k}} i\left(d_{ijm} - d_{imj}\right) k^i S^j_{-\mathbf{k}} S^m_{\mathbf{k}}$, the symmetric component $S$ does not contribute. The resulting Hamiltonian is thus $\sum_{\mathbf{k}} i D \varepsilon_{ijm} k^i S^j_{-\mathbf{k}} S^m_{\mathbf{k}}$, which reproduces the DM interaction in (5.6).

The same method applies to any other lattice. If $S_{-\mathbf{k}}$ and $S_{\mathbf{k}}$ have the same index, its contribution to the Hamiltonian vanishes when completing the summation over momenta. The relevant terms are 6 components of $d_{xyz}$ permutations, and other 12 components of $d_{xxy}$, $d_{xyx}$ and their permutations. For future convenience, these components are symmetrized as $d_{xyz} = \alpha_S + \alpha_A$, $d_{yxz} = \alpha_S - \alpha_A$, $d_{yzx} = \beta_S + \beta_A$, $d_{xzy} = \beta_S - \beta_A$, $d_{zxy} = \gamma_S + \gamma_A$, $d_{zyx} = \gamma_S - \gamma_A$, and $\xi_{\alpha\beta} = d_{\alpha\alpha\beta} - d_{\alpha\beta\alpha}$. As a result, the total Hamiltonian is given by

$$E = \int d^3\mathbf{r} \Bigg[ J\left(\nabla \mathbf{S}\right)^2 - \mathbf{B}\cdot\mathbf{S} + \gamma_A \mathbf{S}\cdot\left(\partial_{\hat{z}} \times \mathbf{S}\right) + \frac{1}{2}\left(\alpha_S + \alpha_A - \beta_S + \beta_A\right)\mathbf{S}\cdot\left(\partial_{\hat{x}} \times S\right) + \frac{1}{2}\left(-\alpha_S + \alpha_A + \beta_S + \beta_A\right)\mathbf{S}\cdot\left(\partial_{\hat{y}} \times S\right) + \xi_{\alpha\beta} S^\beta \partial_\alpha S^\alpha \Bigg] \tag{5.9}$$

where $\partial_{\hat{r}}$ is the directional derivative along $\mathbf{r}$ direction. These linear order derivative terms are the DM interactions. Under low magnetic field $\mathbf{B}$, a spin helix is thus formed along certain directions given the competition between anisotropic DM interaction and the Heisenberg exchange. The last term in this energy characterizes Neel type helices and skyrmions, where the magnetic moments are coplanar with the propagation direction, while the rest of the DM terms belong to the Bloch type, where moments and propagation direction are always perpendicular to each other. A complete list of point groups contributing to nonzero DM interactions is summarized in the following table (Table 5.1).

The inversion symmetry is lost in any of the classes. In addition, the mirror symmetry is also missing in a large portion of the allowed point groups, especially in the cubic crystal system. Higher order spin anisotropies can be constructed in the same way. Once elevated, they might change the ground state, such as anti-vortex state in $S_4$ and $D_{2d}$ once easy axis is established [34, 37]. The B20 compounds, harboring typical Bloch skyrmions, are located in class B-IV. The most important message delivered from this derivation is that class B-V, the $O$ group, is described by exactly the same Hamiltonian as the B20 compounds in class-IV. The spin anisotropies are also the same in these two classes. Therefore the spin physics observed in B20 compounds are also persistent in the $O$ group. A promising family of magnetic skyrmions, $A_2Mo_3N$ with A=Fe, Co, Rh, and their alloys is found [35]. Interestingly, the pure $Co_2Mo_3N$ shows antiferromagnetic behavior and an unexpected superconducting phase in $Rh_2Mo_3N$ at a critical temperature 4.4 K is also found. Searching skyrmion materials in inversion-asymmetric magnets is a cutting edge topic in magnetism [38].

**Table 5.1** Constraints of nonzero $d_{ijk}$ parameters for all possible point groups to create DM interactions. Data is taken from [35]

| Class | Constraints | Point groups |
|---|---|---|
| Block type $\xi_{\alpha\beta} = 0$ | | |
| B-I | No constraints | $D_2$ |
| B-II | $\alpha_S = \beta_S = \gamma_S = 0$ | $D_4, D_3, D_6$ |
| B-III | $\alpha_A = \beta_A = \gamma_A = 0$ | $D_{2d}$ |
| B-IV | $\alpha_S = \beta_S = \gamma_S$, $\alpha_A = \beta_A = \gamma_A$ | $T$ |
| B-V | $\alpha_S = \beta_S = \gamma_S = 0$, $\alpha_A = \beta_A = \gamma_A$ | $O$ |
| Neel type $\alpha = \beta = \gamma = 0$ | | |
| N-I | $\xi_{112} = \xi_{221} = \xi_{331} = \xi_{332} = 0$ | $C_{2v}$ |
| N-II | $\xi_{113} = \xi_{223}, \xi_{112} = \xi_{221} = \xi_{331} = \xi_{332} = 0$ | $C_{3v}, C_{4v}, C_{6v}$ |
| Mixed type | | |
| M-I | No constraints | $C_1$ |
| M-II | $\alpha = \beta = \alpha = 0$, $\xi_{113} = \xi_{223} = 0$ | $C_{1h}$ |
| M-III | $\alpha_A = \beta_A = \gamma_A = 0$ $\xi_{112} = \xi_{221} = \xi_{331} = \xi_{332} = 0, \xi_{113} = -\xi_{223}$ | $S_4$ |
| M-IV | $\alpha_S = \beta_S = \gamma_S = 0$ $\xi_{112} = \xi_{221} = \xi_{331} = \xi_{332} = 0, \xi_{113} = -\xi_{223}$ | $C_3, C_4, C_6$ |

## 5.4 Magnetic Skyrmions in Confined Geometries

As discussed in the first section that the skyrmion-based device is based on the controllable manipulation of individual skyrmions in nanostructured chiral magnets (see Fig. 5.5), particular attention in the field of skyrmions is now focusing on isolated skyrmions in confined geometries. This section will discuss the fabrication of nanostructured samples, real space observation of skyrmions, stability and high flexibility of highly geometrically-confined skyrmions.

### *5.4.1 Sample Fabrication Techniques*

Nanostructured samples can be fabricated by a top-down method from the bulk by using the dual-beam system (Helios Nanolab, 600i FEI, see Fig. 5.7a), i.e. the focused ion beam (FIB) and scanning electron microscope (SEM), combined with a

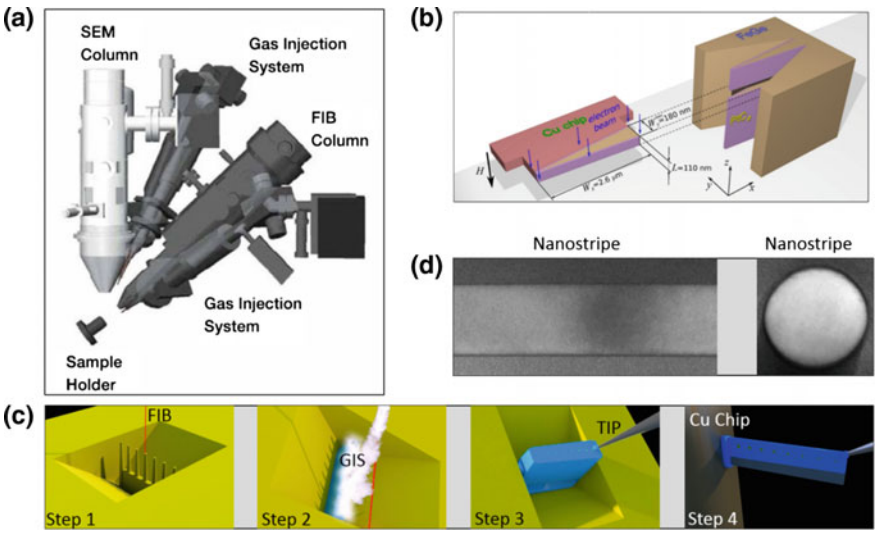


**Fig. 5.7** **a** FEI Helios Nanolab 600i System. **b** A schematic of fabricating a wedged-shape FeGe nanostrip that is chosen to study highly geometrically-confined effect on the skyrmion morphology by using off-axis electron holography and Lorentz TEM, as discussed below. The detailed sample fabrication is shown above. In the TEM measurements, the magnetic field induced by controlling the strength of current in object lens is always along the electron beam direction. Both the dimensions of sample and the coordinate system are marked. **c** Schematic procedure for fabricating nanodisk by using FIB-SEM system. **d** TEM images for the final nanostrip and nanodisk. Images are taken from [24, 49]

Gas Injection System (GIS), and Micromanipulator (Omniprobe 200+ , Oxford) [39]. Dual Beams system consists of a high-resolution SEM column with a fine-probe ion source (FIB). These instruments allow the preparation of samples from specific areas of a sample as well as nano-machining. The OmniProbe AutoProbe™ 200 in situ sample lift-out system allows the preparation of site specific TEM samples without the need for support films. Figure 5.7b represents briefly the fabrication process of wedged nanostrip for the transmission electron microscopy (TEM) observation. In detail, the whole process is schematically depicted in Fig. 5.7c through Fig. 5.4 steps.

**Step 1**: Carving a row of FeGe columns on the surface of a FeGe bulk by using FIB with 30 kV voltage. The process is similar to the procedure to fabricate a TEM specimen [40]. The diameter is designed to be tens to hundreds of nanometers depending on the requirements. In this process, a thin amorphous layer with a thickness of 20 nm will be produced because of the damage of high energy Gallium ions. The amorphous surface is further reduced to 2–4 nm by using low energy Gallium ions with 2–5 kV voltage.

**Step 2**: Coating the FeGe columns with an amorphous $PtC_x$ film. This process is accomplished by combining the Gas Injection System (GIS) and FIB-SEM dual beams. It should be noticed that this amorphous $PtC_x$ is not a magnetic material so that it will not affect the magnetic properties of FeGe sample. The coating layers can

significantly reduce the Fresnel fringes around the sample edges to make it possible to image the magnetic structure of nanostructured sample by using Lorentz TEM.

**Step 3**: Transferring the sample into a silicon surface by using an advanced lift-out method with the help of Omni probe 200+ Micromanipulator that possesses rotation function. In this process, the thin flake is first carved to U-shape and then stuck to the need tip of Micromanipulator. Then, the FeGe sample coating with two $PtC_x$ layers is released from the needle to the surface of the silicon.

**Step 4**: Transferring the sample into Cu-Chip for further fabrication by recycling the steps 1–3.

By slightly changing the procedure including the sample shape and size, a variety of TEM specimens such as nanostrip, nanodisk and wedged films are all able to be fabricated (Fig. 5.7d).

### *5.4.2 Lorentz TEM*

Imaging magnetic skyrmions in real space is highly desired to understand the basic properties of individual skyrmions in confined geometries. The first real space observation of magnetic skyrmions is accompanied by Lorentz TEM [9]. Since then, almost every magnetic imaging technique has been used to investigate the static and dynamical behaviors (Table 5.2). For example, magnetic force microscopy takes advantage of both the short-range interatomic and long-range magnetostatic interactions between the sharp probe and the magnetic material surface. It has been used to help unveiling the magnetic monopole [12]. Magneto-optical effects originate from the interaction between polarized light and the magnetization and have been used to image the formation of individual skyrmions via geometrical confinement [16]. Pump-probe X-ray transmission electron microscope has high temporal resolution and has been used to studying the inertia effect of skyrmions. A large effective mass of magnetic skyrmion was obtained and attributed to the intrinsic breathing mode that acts as a collective source for inertia [41].

Given the size of individual magnetic skyrmions is commonly 3–150 nm, imaging the complex magnetic structure in nanostructured elements require spatial resolution and sensitivity. TEM-based magnetic imaging technique has then obvious advantages. Traditionally, there are two methods to obtain the magnetic signal in the TEM. They are Lorentz TEM and electron holograph (EH), respectively, as shown in Fig. 5.8.

Lorentz TEM relies on the fact that a high energy beam electron will be deflected by the magnetic induction inside and around the magnetic sample [42]. There are two modes in Lorentz microscopy: the Fresnel mode, in which domain walls and magnetization ripples are observed, and the Foucault mode, where domains are imaged. For the Fresnel mode, the minimum observed contrast indicates the in-focus position of the sample. In this position, the domain walls do not appear. Thus out-of-focus conditions by defocusing the objective lens are used to obtain the magnetic contrast of domain walls (see the schematic electron path through the sample in Fig. 5.8a).

**Table 5.2** Magnetic imaging techniques

| Name | Resolution | | Magnetic field | Temperature | Remarks |
|---|---|---|---|---|---|
| | Spatial | Time | | | |
| *Lorentz TEM* | *2* nm | ms | *–0.2–2* T | *5–300* K | *Detect magnetic moments In-plane components (Thin films)* |
| MFM | 10 nm | s | –16–16 T[a] | 2–300 K[a] | Detect the leakage magnetic field |
| SP-STM | Atomic | s | –9–9 T[a] | Low | Magnetic moments atomic smooth in sample surface |
| X-ray Holography | 20 nm | ns | Integrated[a] | Unknown | Magnetic moments ultra-fast dynamics |
| SMOKE | 300 nm | ns | –9–9 T[a] | 2–300 K[a] | High sensitivity Surface detection |
| PEEM | 5 nm | s | 0 T | Room | High sensitivity only surface detection (1–2 nm) |

[a]It indicates the parameters can be conveniently adjusted

To illustrate the principle of Fresnel mode, we only consider a sample composed by two domains with a 180º domain wall in the following.

An electron moving through a region of space with an electrostatic field and a magnetic induction field B experiences the Lorentz force F: $F = e(\mathbf{v} \times \mathbf{B})$, where **v** is the velocity of the electron. F acts normal to the travel direction of the electron, a deflection will occur. Note only components of the magnetic induction normal to the electron beam give rise to a deflection. The deflection angle is linked to the in-plane magnetization and the thickness of the sample. The Lorentz force from the magnetic specimen acts on the electrons passing through the specimen and splits each of the diffraction spots into two (as shown schematically in the Fig. 5.8a). One split spot contains information from domains with magnetization lying in one direction, and the other spot contains information from the antiparallel domains. Under in-focus conditions, there is no magnetic contrast because these deflecting electrons

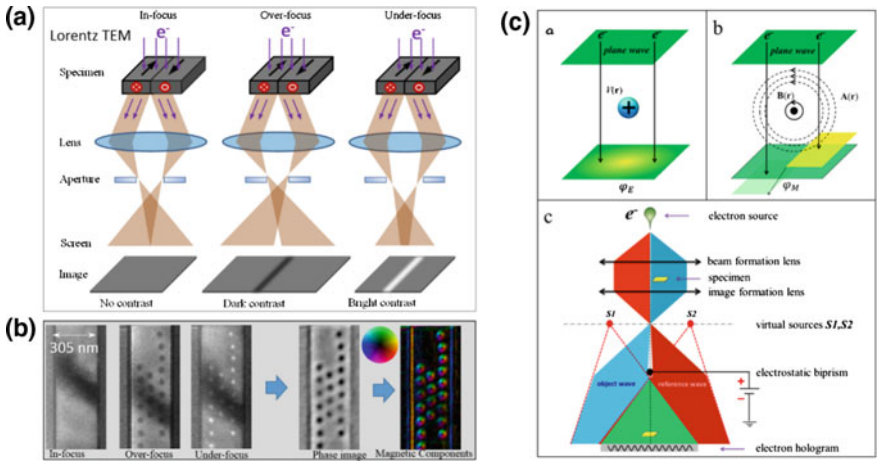


**Fig. 5.8** **a** Ray diagram illustrating the Fresnel image of a magnetic thin plate composed by two 180° domain walls. **b** A real process of reconstructing the in-plane components of a FeGe nanostrip by using the TIE method. The defocus values used in these images are 196 μm $\Delta z = 196\,\mu$m. **c** Schematic diagrams showing different contributions to the electron-optical phase shift arising from local variations in electrostatic scalar potential and magnetic vector potential measured using off-axis electron holography. Electrostatic phase contribution $\varphi_E$ originating from the electrostatic potential $V(r)$ within and around the TEM specimen. Magnetic phase contribution $\varphi_M$ originating from the magnetic vector potential $\boldsymbol{A}(r)$ within and around the TEM specimen. Simplified ray diagram for off-axis electron holography. Essential components are the coherent electron source, electromagnetic lenses and electrostatic biprism for separation and overlap of two parts of the electron wave to form an electron hologram. The object and reference waves can be considered as originating from two virtual sources *S1* and *S2*. The electron-transparent specimen occupies approximately half of the field of view. For recording information about the magnetic properties of the specimen, the conventional TEM objective lens is normally switched off and a non-immersion Lorentz lens is used as the primary imaging lens. A pre-calibrated magnetic field can then be applied to the specimen in the electron beam direction by exciting the conventional objective lens slightly. The final electron hologram can be recorded digitally for further analysis to yield information about the projected electromagnetic potential within and around the specimen. Images are taken from [24, 49]

are finally focused in the image plane. Under out-of-focus conditions, the magnetic domain walls are imaged as alternate bright (convergent) and dark (divergent) lines depending on the over-focus conditions. The bright lines occur when the domain walls are positioned such that the magnetization on either side deflects the electrons toward the wall. This means that the inversion of the magnetic contrast in the domain wall will be observed when we transfer the over- and under-focus conditions. This is a common feature in the Fresnel mode images.

From the above discussion that the magnetic contrasts at the domain wall depend on the defocused conditions, it is thus possible to reconstruct the in-plane distribution of magnetic components around the domain walls. A commercial software package QPt has been developed to realize the purpose based on the transport-of-intensity

equation (5.10) (TIE), where three magnetic images at three defocus values (under-, in-, and over-focus) were used.

$$\frac{2\pi}{\lambda}\frac{\partial I(x,y)}{\partial z} = -\nabla_{xy}.\left[I(x,y)\,\nabla_{xy}\phi(x,y)\right] \tag{5.10}$$

where $I(x, y)$ and $\phi(x, y)$ are the intensity and phase distributions of propagating wave distribution, respectively and $\lambda$ is the electron wavelength. The desired magnetization **m** of the sample is further obtained by the Maxwell-Ampére equations with the relationship

$$\mathbf{m} \times \mathbf{n} = -\frac{\hbar}{et}\phi(x,y) \tag{5.11}$$

where $e$, $\hbar$ and $t$ are the electron charge, the reduced Planck constant and the thickness of the sample, respectively. **n** is the unit vector along the beam direction. The intensity gradient $\partial I/\partial z$ can be approximately expressed as $\Delta I/\Delta z$, because the defocus step $\Delta z$ is usually much less than focal length. Here, a representative process to map the in-plane magnetic components of skyrmions in a nanostrip is illustrated in Fig. 5.8b.

While Lorentz TEM provides a high spatial resolution to image small skyrmions, it is still very hard to observe small samples. This occurs because of the Fresnel fringe effect. Under out-of-focus conditions, the abrupt change of the projected electromagnetic potentials or sample thickness in the sample will inevitably lead to Fresnel contrast, which is more obvious around the sample edge [43]. In this sense, the ability of directly observing the fine magnetic structure by using Lorentz TEM in Fresnel model assumes that the thickness variation or projected electrostatic potentials are negligibly small as compared with the magnetic induction contributions [44]. This is obviously not true around the specimen edges, the abrupt change in thickness leads to significant variation in Fresnel fringes, smearing out the real magnetic contrast. The analysis of magnetic information at the edge is thus extremely difficult. Previous Lorentz TEM investigations on FeGe thin plates have illustrated the artificial contrast extends above ~100 nm[26]. Concerning the helical period of FeGe studied here, it is ~70 nm. This is sufficient to completely eradicate or severely distort the real domain structure of the edge of interest. By contrast, if the nanostructured samples such as nanodisk and nanostrip are coated by amorphous $PtC_x$, the Fresnel fringes effect will be significantly decreased because of the negligible thickness variation, making it possible to observe nanostructured samples.

### 5.4.3 *Off-Axis Electron Holography for Imaging Magnetic Contrast*

According to the Ehrenberg-Siday-Aharonov-Bohm (ESAB) effect in quantum mechanics, the wave function of an electrically charged particle is affected by the

electromagnetic potential through which it traverses. In TEM, the phase change of an electron wave that traverses an electron-transparent specimen (written in one dimension here for simplicity) can be expressed in the form

$$\varphi_{EM}(\mathrm{x}) = \varphi_E + \varphi_M = C_E \int V(x,z)\,dz - 2\pi\frac{e}{h}\iint B_\perp(x,z)\,dxdz, \qquad (5.12)$$

where $x$ is a direction in the plane of the specimen, $z$ is the incident electron beam direction, $C_E$ is an interaction constant that takes a value of $6.53 \times 10^6$ rad·V·m$^{-1}$ at a microscope accelerating voltage of 300 kV, $V$ is the electrostatic potential within and around the specimen and $B_\perp$ is the in-plane component of the magnetic induction within and around the specimen. The total recorded phase $\varphi_{EM}$ is the sum of the electrostatic contribution to the phase $\varphi_E$ originating from the electrostatic potential $V(r)$ (see the left-top panel in Fig. 5.8c) and the magnetic contribution to the phase $\varphi_M$ (see the left-bottom panel in Fig. 5.8c).

One of the most widely used techniques for recording the total phase $\varphi_{EM}$ within and around a specimen directly is the TEM mode of off-axis electron holography. The technique requires the use of a highly coherent field emission gun (FEG) electron source to examine a specimen, in which the region of interest is positioned so that it occupies approximately half of the field of view. The application of a voltage to an electron biprism results in overlap of part of the electron wave that has passed through vacuum alone with part of the same electron wave that has passed through the specimen, as shown schematically in right panel in Fig. 5.8c. If the electron source is sufficiently coherent, then an interference fringe pattern (an electron hologram) is formed in the overlap region, in addition to an image of the specimen. The amplitude and the phase of the specimen wave are encoded in the intensity and the position, respectively, of the interference fringes. For studies of magnetic materials, a Lorentz lens (a high-strength minilens) allows the microscope to be operated at high magnification with the objective lens switched off and the sample located in magnetic-field-free conditions. An external magnetic field can then be applied to the specimen either by using a magnetizing specimen holder or by exciting the conventional microscope objective lens to a pre-calibrated value.

It should be noted that the total phase change $\varphi_{EM}$ is generally a sum of the electrostatic contribution to the phase $\varphi_E$ arising from local variations in specimen thickness and composition and the magnetic contribution to the phase $\varphi_M$ arising from the magnetic vector potential associated with the specimen. Since the magnetic phase information is of primary interest, $\varphi_M$ has to be separated from $\varphi_E$, especially close to the edge of the nanostructure, where the specimen thickness and composition change rapidly. This can be obtained by substracting two phase shifts at two temperatures that are below and above the Curie temperature of magnetic material, respectively bacause the electrostatic contribution to the phase $\varphi_E$ can be recorded as the temperature is above the Curie temperature.

### 5.4.4 Edge-Mediated Skyrmion Phase and Field-Driven Cascade Phase Diagram

With the advance in the nanostructured sample fabrication and imaging technology, it is possible to study the creation, stability and morphology of highly geometry-confined magnetic skyrmions. These contents are in turn discussed in this and next sections and closely related to the non-trivial topology of magnetic skyrmions. It is well known that topological charge is a constant of motion in the space of continuous functions. Therefore, by changing the spin texture from a ferromagnetic or collinear state to a skyrmion state, we must change the topological charge. It is hard to be realized due to an energy barrier, but can be realized in nature by defects or edges initiating Bloch points or other discontinuous states, facilitating the switch of the topological charge. This claim is based on topologically protected property of skyrmion states. More precisely, in geometrically confined systems (such as nanowires), skyrmion configurations are not topologically protected and a transition between uniform and skyrmion state would not be facilitated via singularity (Bloch Point)—they can always be created or destructed at the boundary [45].

This behavior is actually what was observed in the nanodisk. To investigate the phase transitions between different topological classes in detail, a FeGe nanodisk with a diameter of $D \sim 270$ nm is fabricated by the above-mentioned top-to-down method. The size of the nanodisk is designed to be about three times larger than the helical period of B20 FeGe, ~70 nm. The morphology of the nanodisk is shown in Fig. 5.9a. The orientation of magnetic field **B**, pointed upward, is marked by red "⊙". The helical ground state is obviously observed at the temperature $T \sim 100$ K, as shown in Fig. 5.9b, in which the dark and bright stripes are the magnetic contrasts standing for the in-plane magnetic moments distributions. Following the above-mentioned TIE method, the in-plane magnetic configuration of the spin helix can be constructed (Fig. 5.1c). The spin helices have four turns and are distorted around the sample edge (Fig. 5.9c, e) due to the spatial confinement leading to the specific form of the boundary conditions [30, 46].

Under the action of magnetic field, the spin orientation of the helical state will be changed, where confined helices with only three turns are formed at $B \sim 142$ mT. The period of interior helical state is almost unchanged ~70 nm (Fig. 5.9d). At $B \sim 162$ mT, the helix will change into elongated skyrmions by shrinking the length of spin helix. These elongated skyrmions are also called bimerons [47] (Fig. 5.9e, n). This process is always accompanied by forming a completed vortex-like edge state according to theoretical prediction. But, it should be noted that the observed vortex-like magnetic contrast around the nanodisk edge is a mixture of real edge state and Fresnel fringe-induced artificial contrast [48]. With further increasing the magnetic field, the elongated skyrmions will reduce their size to circular shape. Interestingly, at the relatively low magnetic field, the new-formed skyrmions always stay together around the sample edge, as shown in Fig. 5.9f. This gives a strong hint that the skyrmions attract each other, and also are attracted to the edge [24, 49].

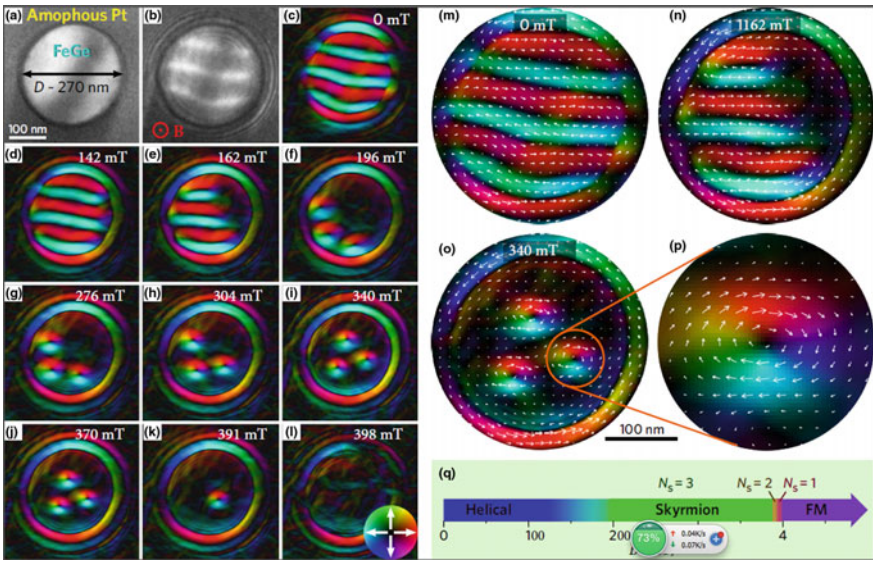


**Fig. 5.9** Magnetic field-driven evolution of magnetic structure in a FeGe nanodisk. **a** TEM image of disk that was coated by non-magnetic PtCx. **b** The spin helix ground state observed by Lorentz TEM. **c–l** Magnetic structure as a function of magnetic field with its orientation pointing outward. The direction and strength of in-plane components are represented by a color wheel in panel (**l**). With the increase of the magnetic field, a spin helix transfers into magnetic skyrmions, which further move to the center of disk and disappear one by one at high magnetic field. **m–o** The enlarged images in panels (**c**), (**d**), and (**i**), respectively. **p**. The fine in-plane magnetic structure for a single skyrmion in panel (**o**) **p**. The magnetic field intervals of hosting varied magnetic structures. $N_s$ represents skyrmion number. Images are taken from [49]

The experimental temperature discussed above is 100 K that is far below the magnetic transition temperature $T_c$ ~280 K [20]. It has been well established that decreasing temperature does not benefit the formation of magnetic skyrmions. For example, in 2D FeGe plates with an approximate thickness of the nanodisk, the lowest temperature of hosting the skyrmion lattice is only about 200 K. Here, the temperature region of hosting magnetic skyrmions extends through the whole interval possible in the experiment. The significantly enhanced stability of skyrmion phase in the highly geometry-confined nanodisk is in sharp contrast to the above-mentioned low stability of skyrmions in bulk [50] and also the thickness-dependent stability in two dimensional films [28]. This phenomenon implies that geometric confinement or sample edge may be used to benefit the formation of magnetic skyrmions. Using the method to calculate the topological charge, we can also project the spin of helical ground state into a sphere. It is found that the surrounding region for the helical ground state with distorted edge twists is much larger than that for a pure ground state. It is actually the distorted edge twists that play a positive role to create skyrmions.

These new-formed skyrmions always stay around the sample edge. With the increase of the magnetic field, the skyrmions move into the center of the disk

with an increased distance of skyrmion-skyrmion and skyrmion-edge, as shown in Fig. 5.9g–j. This common behavior is always observed in the nanodisk with varied diameter and can be readily explained by the repulsive interactions of skyrmion-skyrmion and skyrmin-edge [51].

Before the annihilation of these skyrmions at highest magnetic field, they form a triangle at a magnetic interval B ϵ [196 mT, 370 mT], as shown in Fig. 5.9i, j. With the slight increase of the magnetic field to 391 mT, two skyrmions disappear instantaneously, as shown in Fig. 5.9k and the left one skyrmion stays in the center of the disk, leaving one skyrmion sitting nearly at the center of the disk due to the skyrmion-edge repulsive interaction (Fig. 5.9k). The single skyrmion is finally destroyed at the higher field 398 mT, as shown in Fig. 5.9l.

As mentioned above, skyrmion is a topologically non-trivial spin texture with unit topological charge. Then, the observed cluster state with varied skyrmion number $N_s$ in the disk belongs to a different topological state. The field-driven cascade transition between them has thus a common means. Recent magnetoresistance (MR) measurements on single B20 MnSi nanowires have also demonstrated the cascade transitions [52]. Interestingly, compared with the cluster state with small number of skyrmions, both the Lorentz TEM observation and MR measurements showed that the cluster state with maximum number of skyrmions, $N_s^m$, had a high stability with wider magnetic field intervals at such low temperature (Fig. 5.9q). By contrast, from numerical simulations based on the calculation of equilibrium state, the magnetic intervals of hosting different skyrmion clusters are more complex and comparable at certain conditions, depending on the disk size [53].

At high temperature, skyrmions behave like balls in a box and form a closely-packed arrangement in the disk. A representative phase diagram at varied temperature and magnetic field is shown in Fig. 5.10. As the temperature $T < 190$ K, skyrmions distribute sparsely and form a cluster state, in which the $N_s^m$ is nearly fixed. In other words, the skyrmions do not accommodate the whole disk plane with closed packed mode as expected theoretically. On the contrary, closely packed skyrmions only form at high temperature $T > 190$ K. Similar behavior was also found for nanodisks of different diameters, and provides evidence that the $N_s^m$ at low temperatures is linearly dependent on the diameter of nanodisk.

### 5.4.5 *High Flexibility of Geometrically-Confined Skyrmions*

Mathematically, a magnetic skyrmion has a nontrivial geometrical aspect with respect to its spins. Its non-trivial topology persists under continuous deformation, indicating the tunable skyrmion morphology. For example, the elongated or shrunk skyrmions show the same unit topological charge (Fig. 5.11). But, the appearance of a non-trivial topological object should physically be to some extent energy favorable. For the skyrmion materials studied here, previous theoretical calculation and real-space imaging on bulk or two-dimensional films have identified that skymions appear in circle shape and condense into crystal lattice with a fixed lattice constant [9, 37].

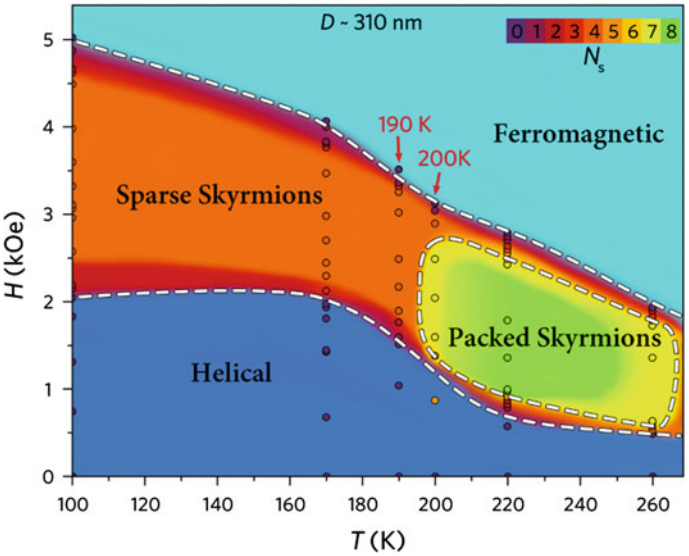


**Fig. 5.10** *Magnetic* phase diagram for a FeGe nanodisk with a diameter of 310 nm. Skyrmions form a cluster state with its maximal number depending on the turn number of initial helical state at low temperature. At high temperature, skyrmions form a closely-packed arrangement. Image is taken from [49]

Accordingly, the benefits of its topological stability are not well exhibited though its topological properties (chirality and winding number) have been manifested by the emergent topological Hall effect [14, 15]. By contrast, as the material dimension is reduced to be comparable to the featured skyrmion size, the topological stability enables a skyrmion to change its shape or size to match the sample geometry. Investigating the skyrmion stability in magnetic nanostructures thus provides a model system to exploit the topological stability under the subject of energy stability.

With the common model describing B20 chiral magnets [27], numerical simulation has confirmed the hypothesis. In detail, consider a nanostripe with a width $W_y$ that is comparable to single skyrmion size and a length $W_x$. Figure 5.12 shows the skyrmion morphology at a middle magnetic field in the nanostripes with varied width. A critical width $W_y^c$ is determined according to the numerical calculations. Below this critical width, skrymions show shrunk shape. Approximately, the morphology of skyrmions can be described by elliptical shape with their semi-axes $a$ and $b$ along and perpendicular to a nanostripe, respectively. Above the critical width $W_y^c$, skyrmions show elongated shape. For a wider nanostripe, two zigzag chains of skyrmions form. It should be noticed that the numerical simulation is based on real nanostripes with certain thickness. For a single layer system, theoretical analysis has demonstrated that elliptical skyrmions would lose its stability from the viewpoint of energy stability.

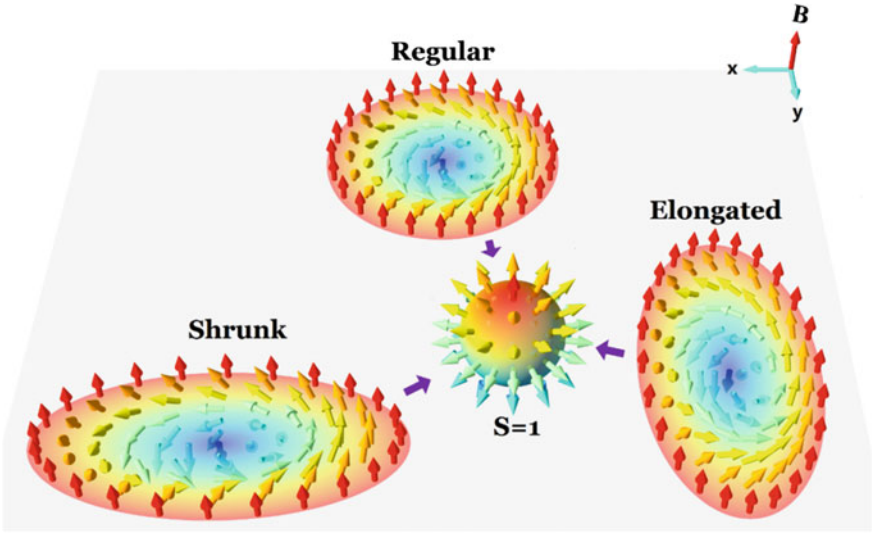


**Fig. 5.11** Schematic representations of topological deformation of magnetic skyrmions by confined geometry. Three kinds of skyrmion configurations (regular, shrunk, and elongated) possess the same unit topological charge, S = 1, because the magnetic moments in these skyrmions can all cover the whole unit sphere only one time

Experimental verification of these elliptical skyrmions has also been done on a wedged-shape sample fabricated by the above-mentioned top-to-down method (Fig. 5.7b). The width of the nanostripe is designed to cross the featured skyrmions lattice constant of FeGe materials (Fig. 5.13a). Due to these ultrasmall sizes, even coating the sample with amorphous $PtC_x$ in the Lorentz TEM cannot obtain the accurate magnetic structure, especially around the sample edge. By contrast, the off-axis EH technique, introduced in Sect. 4.2, uses the in-focus condition to make it possible to accurately map the magnetic induction of nanostructured sample with its size as small as tens of nanometers. This advance provides a unique opportunity to test the predicted existence of twisted edge states [55, 56].

At zero magnetic field, the nanostripe shows a helical ground state with complex arrangements (Fig. 5.13b). Under the action of magnetic field, the spin helices follow the common evolution of helical magnets and change into skyrmions. Due to the strong spatial confinement, only a chain of skyrmions appears (Fig. 5.13c). Similar to the numerical results, shrunk, circular and elongated skyrmions appear in turn with the increase of the width of nanostripe. As the size of skyrmions will decrease with the increase of magnetic field, two chains of skyrmions at the wide part of the nanostripe appear at high magnetic field (Fig. 5.13d). Notably, skyrmions in the narrow part of the nanostripe disappear or migrate at high magnetic field. This implies that the stability of individual skyrmions in confined geometries depends on the dimension of the sample. Moreover, a complete chiral edge twist, characterized by a single-twist rotation of magnetization, is directly observed in the induction maps [57]. Physically,

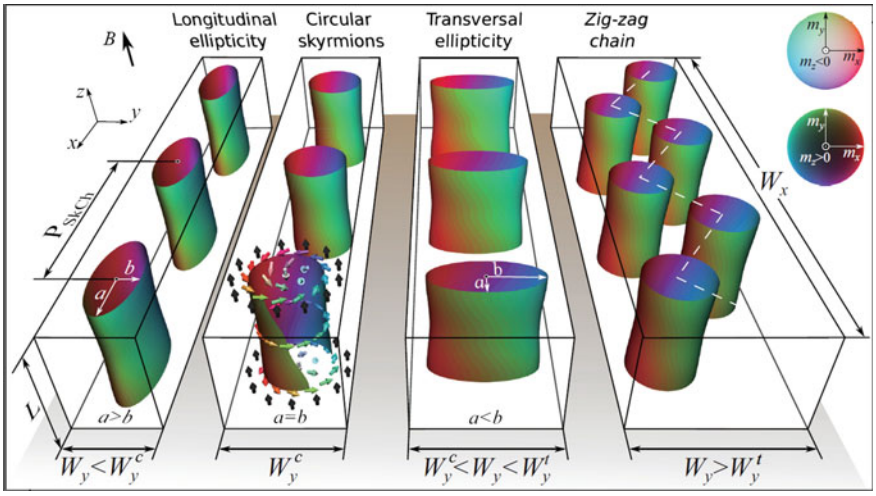


**Fig. 5.12** Skyrmion morphology with varied width for nanostripe with width $W_y$, length $W_x$ and thickness $L$. The magnetization with its three components $m_x$, $m_y$ and $m_z$ is presented by two color wheels. For clarity, only isosurfaces for $m_z = 0$ are plotted. Skyrmions in the nanostripe form a nonhomogeneous tube with varied shape from longitudinal to transversal ellipticity with the increase of the sample width. The color wheel stands for the strength and direction of the in-plane magnetization at each point. Images are taken from [54]

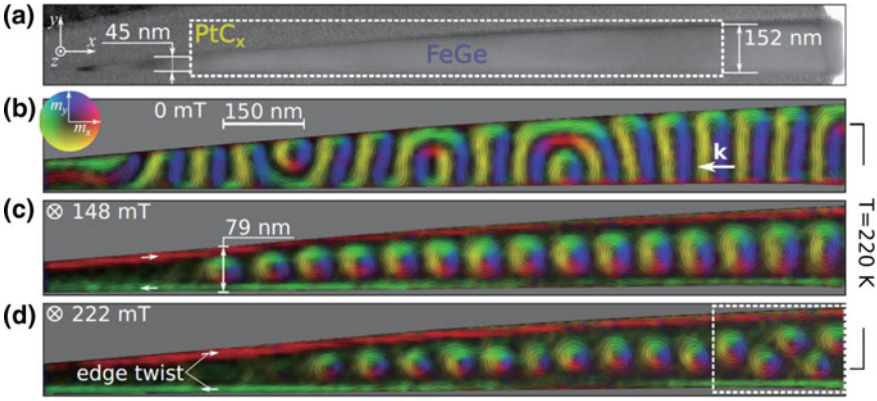


**Fig. 5.13** Skyrmion arrangments in a FeGe nanostripe with varied width at T = 220 K. **a** TEM image of the wedge-shaped FeGe nanostripe. The white frames are the regions chosen for the off-axis EH measurements. The magnetic field points downward represented by the symbol "⊗". **b–d** field-driven evolution of spin textures in such a nanostripe. Skyrmions with controllable morphology are clearly observed

such an edge state represents a type of surface state in a chiral magnet to preserve the magnetic chirality of the whole spin texture.

## 5.5 Conclusions

We have completed a brief introduction through the field of magnetic skyrmions. Starting from a description of limitation of present magnetic memory devices, we have introduced implications of magnetic skyrmions. The demands of skyrmion-based devices require the exploration of new skyrmion materials and understanding of the mechanisms for the formation and stability of geometrically-confined skyrmions.

**Acknowledgements** This work was supported by the National Key R&D Program of China, Grant No. 2017YFA0303201; the Key Research Program of the Chinese Academy of Science, KJZD-SW-M01; the Natural Science Foundation of China, Grant No. 51622105, 11474290; the Key Research Program of Frontier Sciences, CAS, Grant No. QYZDB-SSW-SLH009; the Youth Innovation Promotion Association CAS No. 2015267; the Major/Innovative Program of Development Foundation of Hefei Center for Physical Science and Technology Grant No. 2016FXCX001.

## References

1. D. Weller, A. Moser, IEEE Trans. Mag. **35**, 4423 (1999)
2. A. Brataas, A.D. Kent, H. Ohno, Nat. Mater. **11**, 372–381 (2012) (and reference therein)
3. S. Parkin, S.-H. Yang, Nat. Nanotechnol. **10**, 195 (2015)
4. H.B. Braun, Adv. Phys. **61**(1), 1–116 (2012)
5. O. Tchernyshyov, G.W. Chern, Phys. Rev. Lett. **95**, 197204 (2005)
6. L. Thomas, M. Hayashi, R. Moriya, C. Rettner, S. Parkin, Nat. Commun. **3**, 810 (2012)
7. T.H.R. Skyrme, Nucl. Phys. **31**, 556 (1962)
8. S. Mühlbauer, B. Binz, F. Jonietz, C. Peiderer et al., Science **323**, 915 (2009)
9. X.Z. Yu, Y. Onose, N. Kanazawa, J.H. Park et al., Nature **465**, 901 (2010)
10. N. Nagaosa, Y. Tokura, Nat. Nanotechnol. **8**, 899–911 (2013)
11. S. Rohart, J. Miltat, A. Thiaville, Phys. Rev. B **93**, 214412 (2016)
12. P. Milde, D. Köhler, J. Seidel, L.M. Eng et al., Science **340**, 1076–1080 (2013)
13. M. Lee, W. Kang, Y. Onose, Y. Tokura et al., Phys. Rev. Lett. **102**, 186601 (2009)
14. A. Neubauer, C. Pfleiderer, B. Binz, A. Rosch et al., Phys. Rev. Lett. **102**, 186602 (2009)
15. N. Kanazawa, Y. Onose, T. Arima, D. Okuyama et al., Phys. Rev. Lett. **106**, 156603 (2011)
16. W.J. Jiang, X.C. Zhang, G.Q. Yu, W. Zhang et al., Nat. Phys. **13**, 162–169 (2017)
17. K. Litzius, I. Lemesh, B. Krüger, P. Bassirian et al., Nat. Phys. **13**, 170–175 (2017)
18. A. Fert, V. Cros, J. Sampaio, Nat. Nanotechnol. **8**, 152–156 (2013)
19. W.J. Jiang, P. Upadhyaya, W. Zhang, G.Q. Yu et al., Science **349**, 283–286 (2015)
20. U.K. Rößler, A.A. Leonov, A.N. Bogdanov, J. Phys.: Conf. Ser. **303**, 012105 (2011)
21. T. Okubo, S. Chung, H. Kawamura, Phys. Rev. Lett. **108**, 017206 (2012)
22. S. Heinze, K. von Bergmann, M. Menzel, J. Brede et al., Nat. Phys. **7**, 713 (2011)
23. K. Shibata, X.Z. Yu, T. Hara, D. Morikawa et al., Nat. Nanotechnol. **8**, 723 (2013)
24. H.F. Du, R.C. Che, L.Y. Kong, X.B. Zhao et al., Nat. Commun. **6**, 8504 (2015)
25. T. Moriya, Phys. Rev. **120**, 91 (1960)
26. X.Z. Yu, N. Kanazawa, Y. Onose, K. Kimoto et al., Nat. Mater. **10**, 106 (2011)
27. F.N. Rybakov, A.B. Borisov, A.N. Bogdanov, Phys. Rev. B **87**, 094424 (2013)
28. X.Z. Yu, J.P. DeGrave, Y. Hara, T. Hara et al., Nano Lett. **13**, 3755–3759 (2013)
29. A.B. Butenko, A.A. Leonov, U.K. Roessler, A.N. Bogdanov, Phys. Rev. B **82**, 052403 (2010)
30. M.N. Wilson, E.A. Karhu, A.S. Quigley, U.K. Rößler et al., Phys. Rev. B **86**, 144420 (2012)
31. S. Seki, X.Z. Yu, S. Ishiwata, Y. Tokura, Science **336**, 198 (2012)
32. A.N. Bogdanov, D.A. Yablonskii, Sov. Phys. JETP **68**, 101 (1989)

33. R.R.Birss, *Symmetry and Magnetism*, vol. III (North-Holland Publishing Company, 1964)
34. A.N. Bogdanov, A. Hubert, Phys. Status Solidi B **186**, 527 (1994)
35. W. Li, C.M. Jin, R.C. Che, W.S. Wei et al., Phys. Rev. B **93**, 060409 (2016)
36. A.N. Bogdanov, A. Hubert, J. Magn. Magn. Mater. **195**, 182 (1995)
37. A.N. Bogdanov, A. Hubert, J. Magn. Magn. Mater. **138**, 255 (1994)
38. W.S. Wei, G.J. Zhao, D.R. Kim, C.M. Jin et al., Phys. Rev. B **94**, 104503 (2016)
39. See the details in the internet: http://www.fei.com/products/dualbeam/helios-nanolab
40. D.C. Beaulieu, Electron beam chemical vapor deposition of platinum and carbon. The thesis for degree master (2005)
41. F. Büttner, C. Moutafis, M. Schneider, B. Krüger et al., Nat. Phys. **11**, 225–228 (2015)
42. J.N. Chapman, J. Phys. D: Appl. Phys. **17**, 623–647 (1984)
43. D.B. Williams, C.B. Carter, *Transmission Electron Microscopy: A Textbook for Materials Science* (Springer, New York, 2009)
44. J.N. Chapman, M.R. Scheinfein, J. Magn. Magn. Mater. **200**, 729–740 (1999)
45. D. Cortés-Ortuño, W. Wang, M. Beg, R.A. Pepper, et al. arXiv:1611.07079 (2016)
46. M.N. Wilson, E.A. Karhu, D.P. Lake, A.S. Quigley et al., Phys. Rev. B **88**(21), 214420 (2013)
47. M. Ezawa, Phys. Rev. B **83**(10), 100408(R) (2011)
48. A.O. Leonov, U.K. Rößler, M. Mostovoy, EPJ Web Conf. **75**, 05002 (2014)
49. X.B. Zhao, C.M. Jin, C. Wang, H.F. Du et al., PNAS **113**, 18 (2016)
50. H. Wilhelm, M. Baenitz, M. Schmidt, U.K. Rossler et al., Phys. Rev. Lett. **107**, 127203 (2011)
51. X. Zhang, G.P. Zhao, H. Fangohr, J.P. Liu et al., Sci. Rep. **5**, 7643 (2015)
52. H.F. Du, D. Liang, C.M. Jin, L.Y. Kong et al., Nat. Commun. **6**, 7637 (2015)
53. H.F. Du, W. Ning, M.L. Tian, Y.H. Zhang, Phys. Rev. B **87**(1), 014401 (2013)
54. H.F. Du, Z.A. Li, A. Kovacs, J. Caron et al., Nat. Commun. **8**, 15569 (2017)
55. J. Sampaio, V. Cros, S. Rohart, A. Thiaville et al., Nat. Nanotechnol. **8**, 839 (2013)
56. J. Iwasaki, M. Mochizuki, N. Nagaosa, Nat. Nanotechnol. **8**, 742 (2013)
57. S.A. Meynell, M.N. Wilson, H. Fritzsche, A.N. Bogdanov et al., Phys. Rev. B **90**, 014406 (2014)